Electronic supplementary information for 'Fragment imaging in infrared photodissociation of Ar-tagged protonated water clusters, H$_3$O$^+$-Ar and H$^+$(H$_2$O)$_2$-Ar'

Yuri Ito, Mizuhiro Kominato, Yuji Nakashima, Keijiro Ohshimo, and Fuminori Misaizu[a]

Department of Chemistry, Graduate School of Science, Tohoku University, 6–3 Aoba, Aramaki, Aoba-ku, Sendai 980–8578, Japan

[a]Author to whom correspondence should be addressed: misaizu@tohoku.ac.jp

1. Improvement in the imaging electrodes

Fig. S1 shows an overview of the imaging apparatus combined with a linear-type double reflectron mass spectrometer. In the previous setup,[1] the 2nd reflectron to analyze photofragment ions consisted of four annular electrodes. By removing a metal mesh from the electrode, an electrostatic lens was formed inside the 2nd reflectron as a velocity map imaging (VMI) configuration.[2] However, an initial position spread of the ions in the photodissociation region was not completely reduced at the detector, especially for the ions with a recoil velocity component along the time-of-flight (TOF) direction.[1] Therefore, the VMI condition cannot be achieved using the annular reflectron electrodes.
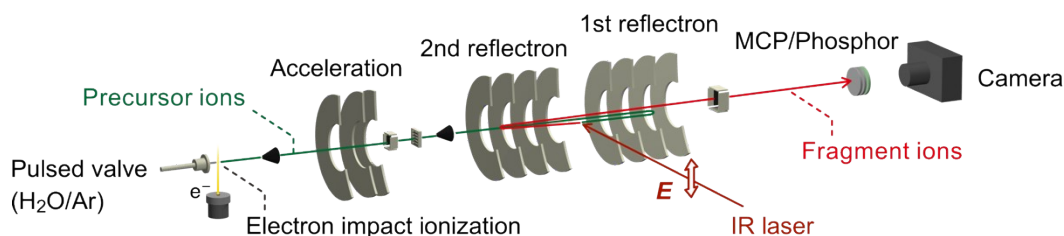

Fig. S1 Schematic overview of the imaging apparatus with a linear-type tandem reflectron. The trajectories of precursor ions and fragment ions are indicated by green and red lines, respectively.

In this study, it was found that a new design of the reflectron electrode can improve the image resolution. Fig. S2a is a cross-sectional view of the improved double reflectron. A "rim" structure was added to the annular electrode for the 2nd reflectron based on the ideas in the previous studies.[3,4] A shape of the rims was optimized as shown in Fig. S2b using ion trajectory simulations with the SIMION 8.1 program.[5] The simulations were started at the dissociation point, that is, the middle point of the double reflectron region, at $(X, Z) = (0, 0)$, where the X axis is defined as a transverse axis to the TOF axis (Z) as indicated in Fig. S2c. Three photofragment ions were placed at $(X, Z) = (-0.5$ mm, 0), (0, 0), and (+0.5 mm, 0) with 700 m/s recoil velocity. Angles of the recoil velocity were set as 0°,

45°, 90°, 135°, and 180° with respect to the Z axis. Simulation results of the ion positions at the detector are shown in Fig. S2d. Utilizing the optimized rims, the ion position spread was fairly reduced. The residual ion spread for the new design resulted in 0.12 mm for the 90° recoil direction, 0.04 mm for 45°/135°, and 0.18 mm for 0°/180°. Therefore, the rim electrodes achieve the VMI condition, where the initial position spread of the ions (1 mm) can be reduced irrespective of their recoil angles.
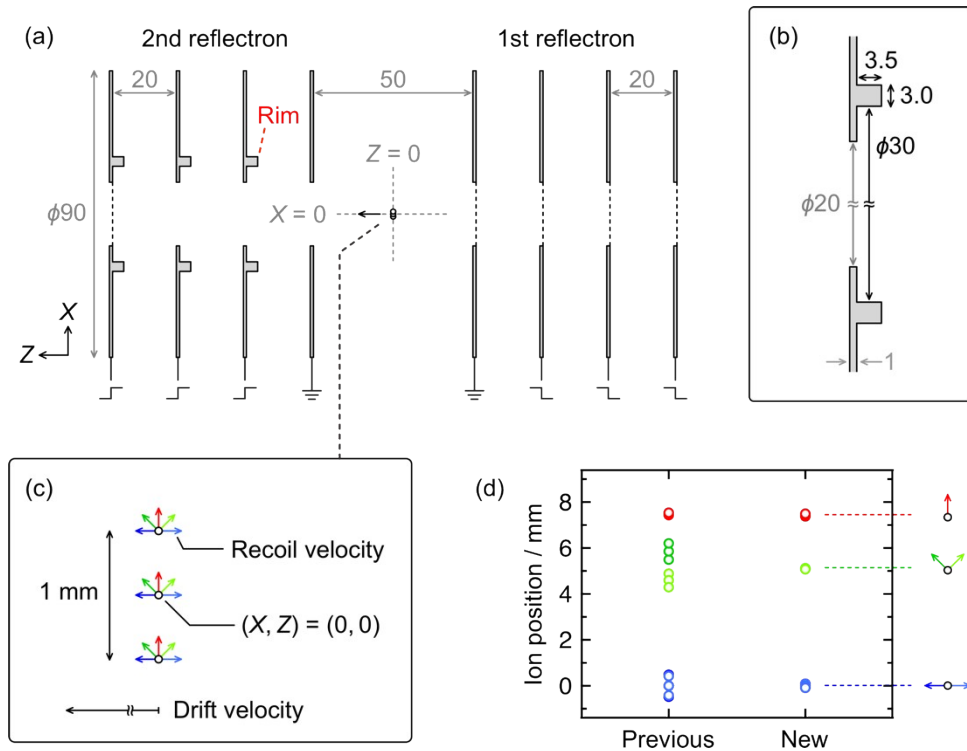

Fig. S2 (a) Entire view of the improved double reflectron. Definitions of the X and Z axes are shown inset. Broken lines on the inner apertures of the electrodes indicate fine metal meshes. (b) Enlarged view for a rim on the electrode. (c) Initial conditions of the photofragment ions in the simulation. Three positions and five recoil directions were chosen as the initial conditions. Therefore, a total of 15 ions were examined in the simulation. (d) Simulated ion positions at the detector for the previous and new designs of the reflectron electrodes. Red, green, and blue plots correspond to the 90°, 45°/135°, and 0°/180° recoil angles, respectively, as indicated inset.

The performance of the new electrodes was experimentally evaluated with 355 nm photodissociation of Ca$^+$Ar. Photofragment Ca$^+$ images for the previous and new reflectron electrodes are compared in Fig. S3a. A more focused image was obtained with the improved apparatus. In the velocity distribution of Ca$^+$ shown in Fig. S3b, the velocity resolution, $\Delta v/v$, was found to be improved from 0.37 to 0.20. The velocity spread in the improved apparatus was $\Delta v = 130$ m/s. The narrowest velocity distribution in the present infrared experiments was $\Delta v \sim 260$ m/s for the v_b^{II} excitation of H$^+$(H$_2$O)$_2$-Ar,

and thus the improved apparatus was confirmed to have enough image resolution.
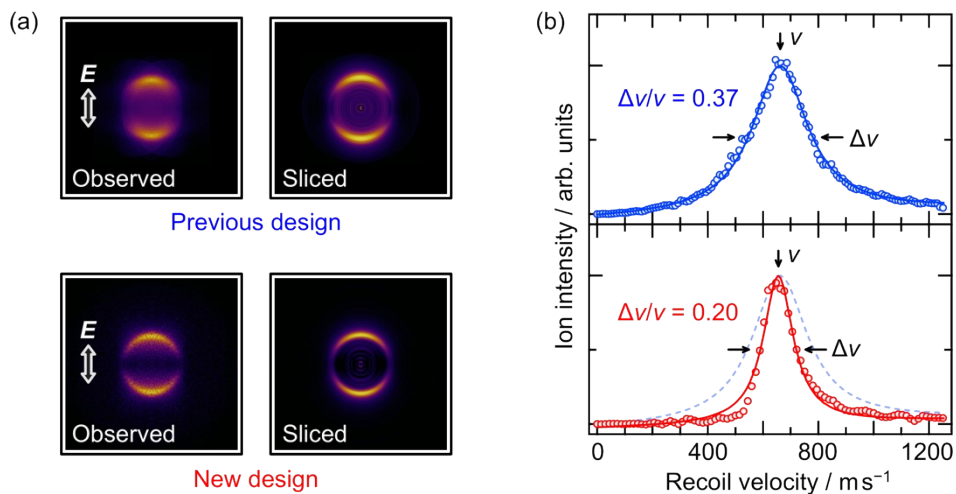

Fig. S3 (a) Observed and pBASEX[6] sliced image of Ca^+ from 355 nm photodissociation of Ca^+Ar recorded with the previous (top) and new (bottom) designs of the electrodes for the 2nd reflectron. *E* denotes the polarization direction of the dissociation laser. (b) Velocity distributions of Ca^+ obtained with the previous (top) and new (bottom) setups. The experimental plots (circles) were fitted with Lorentzian functions (curves). In the velocity distribution plot for the new design, the fitting result for the previous one is also shown for comparison.

2. Results of the spectral simulation

Spectral simulations for the ν_f^I band of H_3O^+-Ar were performed with the PGOPHER program[7] to estimate the rotational temperature, T_{rot}. In the simulation, H_3O^+-Ar was treated as an asymmetric top in the C_{2v} point group. Rotational constants were determined from the optimized structure at the MP2/aug-cc-pVTZ level as $A = 10.6$, $B = 0.14$, and $C = 0.14$ cm^{-1}. Simulated spectra were convoluted with a Lorentzian function of FWHM = 4 cm^{-1} to consider the experimental resolution. Fig. S4a and S4b show simulated spectra for $T_{rot} = 20$–100 K and $T_{rot} = 40$–60 K, respectively. The experimental spectrum is also shown in Fig. S4c for comparison.
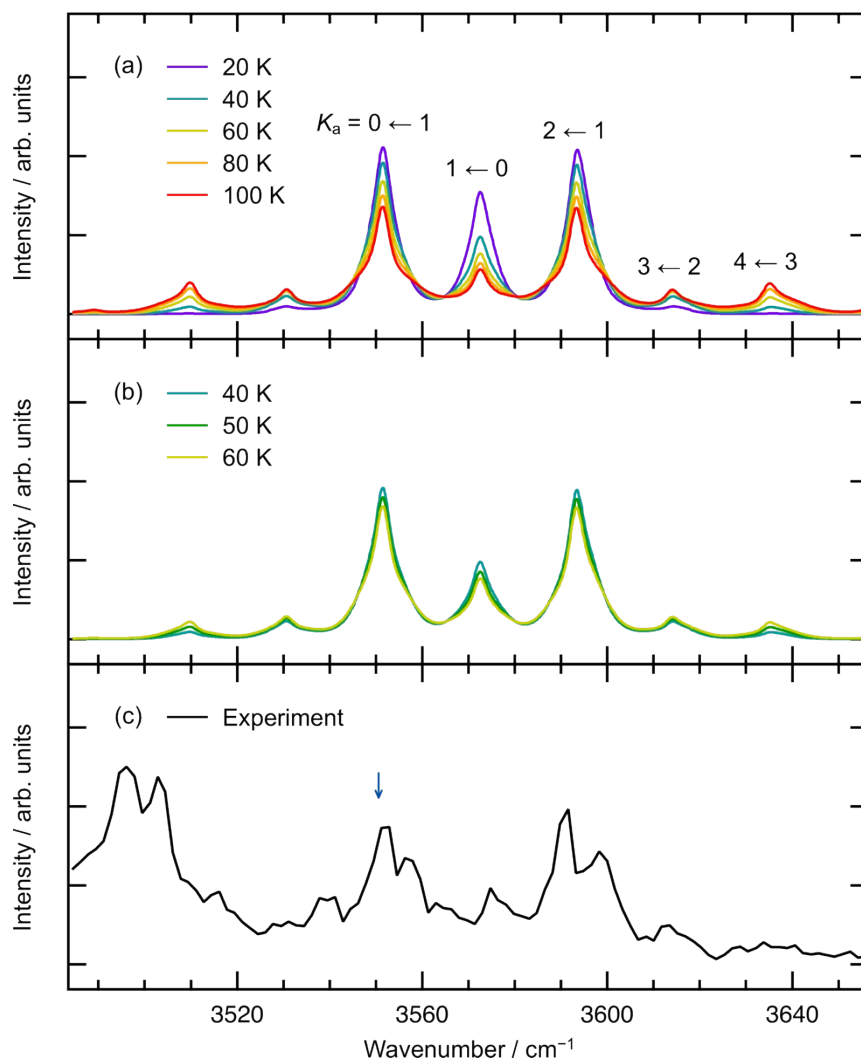

Fig. S4 Simulated ν_f^I band of H_3O^+-Ar at (a) 20–100 K, (b) 40–60 K, and (c) the experimental spectrum. See the text for details of the spectral simulation. An arrow on the experimental spectra indicates the $K_a = 0 \leftarrow 1$ sub-band chosen for the imaging experiment.

The splitting pattern in the v_f^I band arises from K_a, which corresponds to K in approximating H_3O^+-Ar to a prolate top. In the spectra simulated at 80 K and 100 K, the $K_a = 4 \leftarrow 3$ sub-band is more intense than the neighboring $4 \leftarrow 3$ sub-band, unlike the experiment. On the other hand, at 20 K, the relative intensity of the $1 \leftarrow 0$ sub-band is somewhat larger than the experiment. Consequently, T_{rot} for the experiment is estimated to be 50 ± 10 K.

Fig. S5a shows a comparison between the experimental spectrum and a simulated spectrum at $T_{rot} = 50$ K for the v_b^I and v_f^I bands. Fig.S5b is simulated intensity plots of the individual rotational lines at 50 K. In these profiles, the most contributing initial state to the band structure was determined to be $(J'', K_a'') = (11, 1)$.
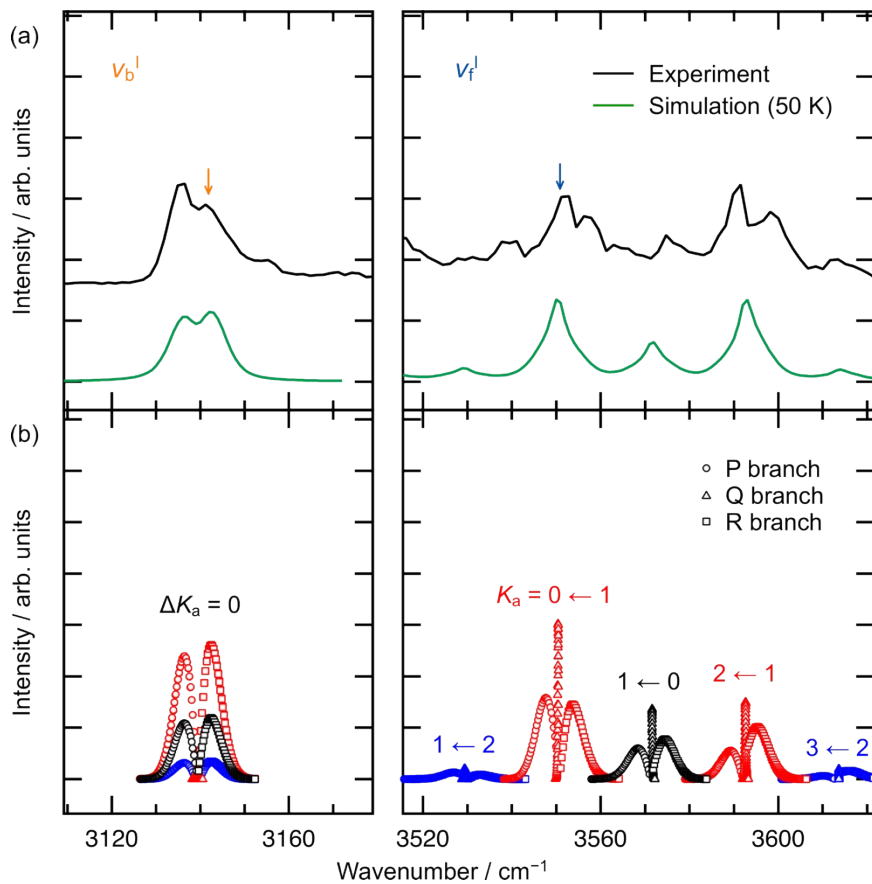

Fig. S5 (a) Comparison of the experimental and simulated spectra for the v_b^I and v_f^I bands of H_3O^+-Ar. Arrows on the experimental plot indicate the excitation energies for the imaging experiments. (b) Profiles of the rotational lines. The simulations were conducted at $T_{rot} = 50$ K.

3. Calculated results of the vibrational modes

Fig. S6a and S6b show normal mode descriptions for the v_b^I/v_f^I modes of H_3O^+-Ar and the v_b^{II}/v_f^{II} modes of $H^+(H_2O)_2$-Ar, respectively. Displacement vectors for each mode were calculated at MP2/aug-cc-pVTZ. Table SI and SII summarize vector profiles for H atoms in H_3O^+-Ar and $H^+(H_2O)_2$-Ar, respectively.
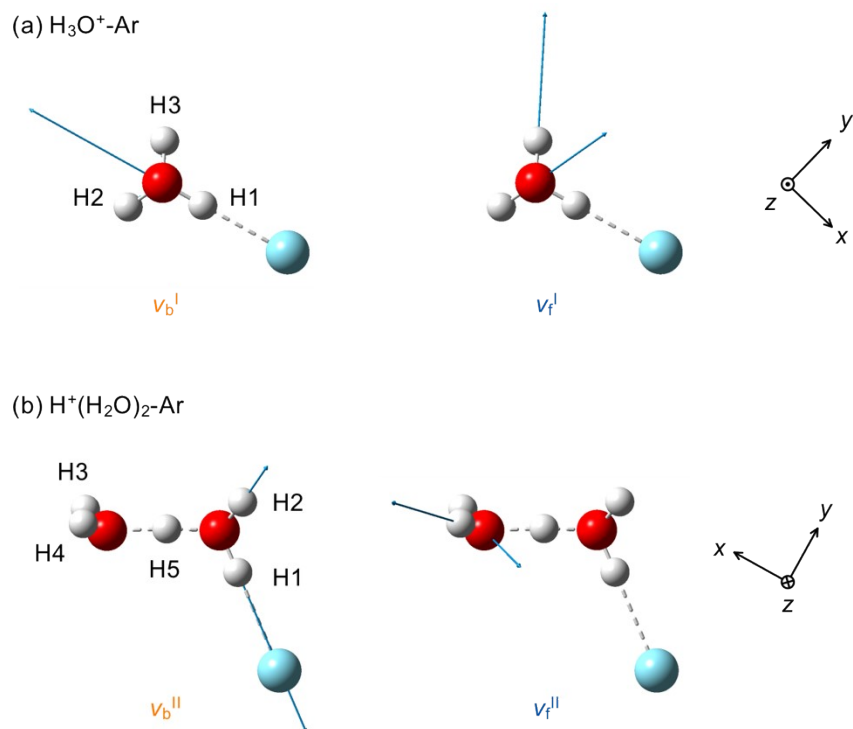
Fig. S6 Illustration for displacement vectors (blue arrows) in (a) H_3O^+-Ar and (b) $H^+(H_2O)_2$-Ar for normal mode descriptions of the v_b and v_f modes calculated at the MP2/aug-cc-pVTZ level. Labels for the H atoms and definitions for the x, y, and z coordinates for Table SI and SII are also shown.

Table S1 Calculated the x, y, and z components for the displacement vectors and amplitudes, $r = (x^2 + y^2 + z^2)^{1/2}$ of the v_b and v_f modes in H_3O^+-Ar. Only the values for the H atoms are shown, and those for the O and Ar atoms are < 0.1 times smaller than the maximum for the H atoms.

Mode	Atom	x	y	z	r
v_b^I	H1	0.99	0.00	−0.05	0.99
	H2	−0.04	0.09	−0.02	0.10
	H3	−0.04	−0.09	−0.02	0.10
v_f^I	H1	0.00	−0.01	0.00	0.01
	H2	−0.28	0.58	−0.28	0.70
	H3	0.28	0.58	0.28	0.70

Table S2 Calculated the x, y, and z components for the displacement vectors and amplitudes, $r = (x^2 + y^2 + z^2)^{1/2}$ of the v_b and v_f modes in $H^+(H_2O)_2$-Ar. Only the values for the H atoms are shown, and those for the O and Ar atoms are < 0.1 times smaller than the maximum of the H atoms.

Mode	Atom	x	y	z	r
v_b^{II}	H1	0.88	−0.37	0.04	0.96
	H2	−0.04	0.24	0.17	0.30
	H3	0.02	0.00	0.02	0.03
	H4	0.01	0.01	−0.02	0.02
	H5	−0.02	−0.02	−0.01	0.03
v_f^{II}	H1	0.00	0.00	0.00	0.00
	H2	0.00	0.00	0.00	0.00
	H3	0.45	−0.01	0.51	0.68
	H4	−0.35	−0.18	0.61	0.73
	H5	0.00	0.00	0.00	0.00

References

[1] K. Okutsu, Y. Nakashima, K. Yamazaki, K. Fujimoto, M. Nakano, K. Ohshimo, and F. Misaizu, *Rev. Sci. Instrum.* **88**, 053105 (2017).

[2] A. T. J. B. Eppink and D. H. Parker, *Rev. Sci. Instrum.* **68**, 3447 (1997).

[3] V. Papadakis and T. N. Kitsopoulos, *Rev. Sci. Instrum.* **77**, 083101 (2006).

[4] S. Trippel, M. Stei, R. Otto, P. Hlavenka, J. Mikosch, C. Eichhorn, U. Lourderaj, J. X. Zhang, W. L. Hase, M. Weidemüller, and R. Wester, *J. Phys.: Conf. Ser.* **194**, 012046 (2009).

[5] D. Manura and D. Dahl, *SIMION 8.0 User Manual* (Scientific Instrument Services, Inc., Ringoes, NJ, 2008).

[6] G. A. Garcia, L. Nahon, and I. Powis, *Rev. Sci. Instrum.* **75**, 4989 (2004).

[7] C. M. Western, *J. Quant. Spectrosc. Radiat. Transfer* **186**, 221 (2017).